Journal of Sustainable Metallurgy (2026) 12:3412–3425
https://doi.org/10.1007/s40831-025-01308-8

THEMATIC SECTION: 9TH INTERNATIONAL SLAG VALORISATION SYMPOSIUM

Investigation of Electrical Conduction in Iron Silicate Slags via Electrical Conductivity Experiments and Iron Redox State Determination

Pieter-Jan Boeykens[1] · Roman Starykh[2] · Iulian Dugulan[3] · Jeff Chen[2] · Maksym Shevchenko[2] · Lennart Scheunis[4,5] · Amy Van den Bulck[5] · Evgueni Jak[2] · Kim Verbeken[1] · Inge Bellemans[1]

Received: 22 May 2025 / Accepted: 8 October 2025 / Published online: 23 October 2025

Abstract

The present work aims to elucidate the influence of the iron oxidation state on the electrical conductivity of iron silicate slags through a combined approach of electrical conductivity measurements and iron redox state determination. Electrical conductivity experiments were combined with stepped potential chronoamperometry measurements to distinguish between the ionic and electronic conduction mechanism. Contrary to previous studies, the Fe^{3+}/Fe^{2+} ratio was also experimentally determined via both Mössbauer spectroscopy and wet chemistry. A continuous decrease in Fe^{3+}/Fe_{tot} ratio was found which varies accordingly to the different atmospheres applied during each experiment which confirmed that the changes in the electrical conductivity are attributed to a difference in the sample's iron redox state. The ionic and electronic conductivity showed a linear and parabolic dependency, respectively, as a function of Fe^{3+}/Fe_{tot}. The experimental data were compared with two models, namely, the structural ionic model of Thibodeau et al. and the electronic Diffusion-Assisted Charge Transfer (DACT) model from Barati and Coley. Regarding the former, it is found that the model overestimates the ionic conductivity due to an overestimation of the Fe^{2+} diffusion coefficient. The latter model was unable to reproduce the experimental data using the original model's original *r** parameter of 3.87 Å, but adaptation of this parameter to 4.67 Å provided a better fit. This suggests that the DACT model also needs to consider a slag composition dependency to accurately reproduce experimental data.

The contributing editor for this article was Hongmin Zhu.

✉ Kim Verbeken
kim.verbeken@ugent.be

✉ Inge Bellemans
inge.bellemans@ugent.be

Pieter-Jan Boeykens
pieterjan.boeykens@ugent.be

Roman Starykh
r.starykh@uq.edu.au

Iulian Dugulan
A.I.Dugulan@tudelft.nl

Jeff Chen
j.chen5@uq.edu.au

Maksym Shevchenko
m.shevchenko@uq.edu.au

Lennart Scheunis
lennart.scheunis@eu.umicore.com

Amy Van den Bulck
amy.vandenbulck@eu.umicore.com

Evgueni Jak
e.jak@uq.edu.au

[1] Ghent University, Ghent, Oost-Vlaanderen, Belgium

[2] University of Queensland, Brisbane, QLD, Australia

[3] Technical University Delft, Delft, Zuid-Holland, The Netherlands

[4] Umicore, Shanghai, China

[5] Umicore N.V., Olen, Antwerp, Belgium

Graphical Abstract

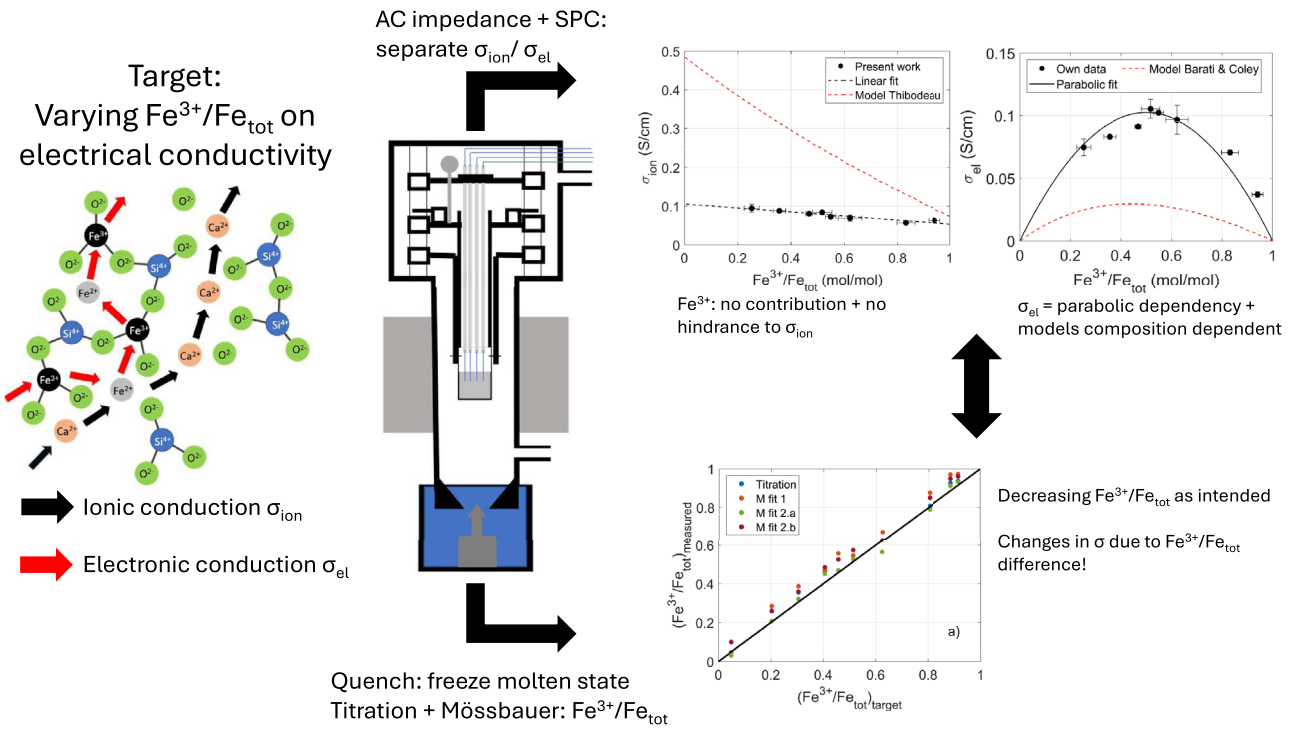

Keywords Pyrometallurgy · Slag · Electrical conductivity · Iron oxidation state

Introduction

Electric furnaces are expected to become increasingly more important in the metallurgy sector due to their potential of reducing greenhouse gas emissions compared to traditional fossil fuel-based furnaces if powered by less carbon intensive and/or renewable energy sources such as nuclear, hydro, wind, or solar power. Within the steelmaking sector, both electric arc furnaces (EAF) and electric smelter furnaces (ESF) will become necessary for refining direct reduced iron (DRI) obtained via the reduction of iron ore or via natural gas and/or hydrogen [1–5]. For the EAF technology though, DRI produced from high-grade ore (Fe > 67 wt%) in combination with steel scrap is needed as these furnaces are not suitable to handle high slag volumes as this would significantly increase electricity consumption and iron losses [4, 5]. On the other hand, an ESF is able to handle DRI produced from lower grade ores as slag formation is beneficial for furnace heating [3–5]. However, the ESF is only an intermediate furnace as it produces molten metal which needs to be subsequently refined in a basic oxygen furnace (BOF) [4, 5]. Nowadays, ESF technology is intensively used within the ferroalloy sector [6–8] and non-ferro slag cleaning [9]. An ESF can be operated in different regimes, namely submerged arc mode, brush arc mode, and shielded arc mode [6]. For the submerged arc regime, heat is generated solely via the conversion of electricity using the slag bath resistance which is known as Joule heating. In brush arc mode, heat is generated both via Joule heating within the slag as well as from the generated electric arc, but with the majority of the heat still being generated in the slag bath. In shielded arc operation, the majority of the heat is generated from the arc. However, the ability to form an arc has also been found to rely on the slag bath resistance with a higher resistance requiring higher voltages and thus making arc formation more challenging to achieve [6, 7, 10]. As the slag resistance is inversely proportional to the slag's electrical conductivity, knowledge on this material property is essential for the operation and design of an ESF.

The focus of this work is on iron silicate slags in which conduction occurs both via the movement of metal cations [11] as well as electron hopping between multivalent cations such as Fe^{2+} and Fe^{3+} [12]. Several previous works [13–23]

Table 1 Starting composition of the slag for electrical conductivity measurements (in mol%)

	CaO	SiO_2	$AlO_{1.5}$	'FeO'
Mol%	33.55	29.75	16.00	20.70

Table 2 Summary of the experimental conditions in terms of applied p_{O2} in the furnace and targeted Fe^{3+}/Fe_{tot} ratio of the slag according to FactSage 7.3 UQPY database [25] for the slag compositions listed in Table 1

	Experimental conditions							
$Log(p_{O2})$	− 0.68	− 2.00	− 4.00	− 5.01	− 5.51	− 5.96	− 6.87	− 7.92
Fe^{3+}/Fe_{tot}	0.89	0.80	0.62	0.51	0.46	0.41	0.31	0.20

have studied the electrical conductivity and/or this mechanism already. However, it should be noted that only a limited number of these studies [17–20] performed an experimental technique, such as stepped potential chronoamperometry (SPC), to separate the ionic and electronic contributions to the total conductivity. In addition, of the abovementioned studies, only Engel and Vygen [15], Hundermark [16], and Zhao et al. [21] checked for the presence of solids and/or changes in the slag composition due to Fe uptake or crucible dissolution via post-experimental characterization techniques. Even more, the iron redox state, Fe^{3+}/Fe^{2+}, was only experimentally verified by Hundermark [16], for a limited number of samples, and by Engel and Vygen [15]. Thus, to the authors' knowledge, no study exists which combines the determination of the slag's iron redox state with an experimental technique to separate both the ionic and electronic conductivity. The present work aims to combine both electrical conductivity experiments and iron redox state determination. Experiments were carried out on synthetic SiO_2–$AlO_{1.5}$[1]–CaO–'FeO' slags as a function of the iron oxidation state using a previously described methodology for electrical conductivity experiments [24], while the iron redox state was measured via both Mössbauer spectroscopy and wet chemistry.

Methodology

Electrical Conductivity Experiments

Synthetic slags were prepared to match the composition as shown in Table 1 and their preparation is similar as described in our previous work [24]. The preparation was done via a two-step process in which first a sinter of CaO–$AlO_{1.5}$–SiO_2 (CAS) is prepared from mixing high-purity powders of $CaCO_3$ (99.9%), Al_2O_3 (99.7%), and crushed SiO_2 glass (99.999%), which are subsequently put in an alumina crucible inside a muffle furnace at 1240 °C overnight. This CAS sinter was then added to Fe_2O_3 powder (99.8%) and Fe powder (99.9%) to obtain the predicted Fe^{3+}/Fe^{2+} ratio for an experiment at a certain p_{O2} as obtained via FactSage 7.3 UQPY database [25]. The quantity of Fe_2O_3 and Fe powder were determined from Eq. (1) assuming that both react stoichiometrically.

$$Fe_2O_3 + Fe \rightarrow 3FeO \tag{1}$$

All powders were thoroughly mixed in a pestle and mortar before being pelletized using a stainless steel die and manual press. For the high-temperature conductivity measurements, a bath height of 25 mm was desired which corresponds to ± 40 g. The amount of slag needed was calculated based on the density/molar volume model of Thibodeau et al. [26–28] using the slag's chemical composition and the experimental temperature. After pelletizing, the pellets were brought into an alumina crucible (99.7% purity) and put inside the electrical conductivity furnace. After this, the furnace was completely sealed off from the surrounding atmosphere, it was flushed with the desired gas composition at a flow rate of 1 l/min for 9 h. The temperature was subsequently increased to 1310 °C at a rate of 5 °C/min and kept for 6 h to allow melting of the powder and homogenization of the bath. The targeted oxygen partial pressure and iron oxidation state can be found in Table 2. From the works of Goldman [29], Pommier et al. [30], and Vergote et al. [31], it is known that the kinetics of Fe^{2+}/Fe^{3+} changes in silicate slags is slow as experiments are typically performed on samples with a limited mass (1 g–10 g) in combination with a large driving force, e.g., placing an oxidized slag in a reducing atmosphere. In addition, measurement times between 6 h and 24 h are needed to observe changes in the Fe^{2+}/Fe^{3+} ratio. The current experiments were carried out for a significantly larger sample mass in combination with an Fe^{2+}/Fe^{3+} ratio close to the equilibrium for the applied gas atmosphere. As such, it is expected that the slag's Fe^{2+}/Fe^{3+} ratio remains constant throughout the experiment.

Electrical conductivity measurements commenced via first determining the bath height and correcting for the formation of a meniscus as described in our previous work [24]. The same procedure for determining the total electrical conductivity and the electronic transference number as in the previous work was done as well. After determination of the bath surface, the electrodes were lowered to an immersion

[1] The authors prefer the use of $AlO_{1.5}$ over Al_2O_3 for the alumina content in the slag system as this gives an easier visualization of the amount of cations in the slag, which are the main contributors to the ionic conductivity. Similarly, 'FeO' is used as the notation for both FeO and $FeO_{1.5}$ and indicates the total Fe cation content regardless of the oxidation state.

depth of 10 mm and a frequency sweep was carried out. The real impedance was frequency-independent over a broad range from 100 Hz to 50 kHz. To determine the electrical conductivity, single frequency measurements were carried out at 10 kHz at immersion depths of 8, 9, 10, 11, and 12 mm starting with the one at 10 mm. The electronic transference number was determined via the SPC technique. The open circuit potential of the system was then recorded for 10 min after which SPC was executed. The system was held at the open circuit potential (OCP) for 1 min prior to a voltage step of − 10 mV (vs OCP) for 40 min during which the current was measured at a scan rate of 100 Hz. After the SPC technique, single frequency measurements were done at the same immersion depths as before to check whether the electrical conductivity changed as a result of the SPC technique and/or crucible dissolution. After the experiment, the crucible was removed from the furnace into a bucket of water to quench the slag which allows subsequent characterization via light optical microscopy (LOM) to determine the presence and location of solid crystals in the slag, investigation of the slag composition via electron probe X-ray microanalysis (EPMA) and X-ray fluorescence analysis (XRF) and the slag's iron redox state via Mössbauer spectroscopy and wet chemistry.

Composition and Iron Redox State Analysis

Composition Analysis

Slag pieces were embedded in Epofix resin and subsequently ground and polished up to 1 µm abrasive size for LOM and EPMA analysis. All elements were measured using the conventional EPMA technique which was performed with an acceleration voltage of 15 keV, a beam current of 20nA, and a probe diameter ranging from 5 to 30 µm depending on the specific phase being analyzed. The following detectors and spectral lines were employed for elemental measurement: Al K_α—TAP, Fe K_α—LIF, Si K_α—PET J, and Ca K_α—PET J. For the measurement of Al, Ca, Fe, Si, and the corresponding cations, pure (synthetic) Al_2O_3, Fe_2O_3, SiO_2, and $CaSiO_3$ standards were used, respectively. All referenced materials were provided by Charles M. Taylor. Raw measured data underwent standard ZAF correction using the Armstrong/Love Scott approach. For each sample, at least 15–20 different spots were chosen from which the average chemical composition could be determined.

Mössbauer Spectroscopy

Mössbauer spectroscopy is chosen as the principal technique for the determination of the iron redox state in this work as this technique is non-destructive and has the potential to provide insights into both the iron oxidation state as well as the coordination number [32–35]. Mössbauer spectroscopy was carried out at the TU Delft Reactor Institute. For this analysis, the slag was first pulverized to a fine powder and about 150 mg was used for each experiment. Transmission ^{57}Fe Mössbauer spectra were collected at 298 K with constant-acceleration or sinusoidal velocity spectrometers, using a ^{57}Co(Rh) source. Several studies report, however, that Mössbauer spectroscopy can overestimate the Fe^{3+} in glasses/melts by up to 15% if no correction is made for the difference in temperature dependency between the recoilless fraction of Fe^{3+} compared to Fe^{2+} [36–38]. This is related to the weaker bond strength of Fe^{2+} compared to Fe^{3+}, which results in a lower Debye temperature θ_D (K), thereby affecting the recoilless fraction of a component as a function of temperature. To check the temperature dependency of the Mössbauer spectra, additional measurements at 20 K and 50 K were carried out for the sample obtained using a p_{O2} of $10^{-5.5}$ atm. As the sample matrix, i.e., CaO, SiO_2, and $AlO_{1.5}$, is constant for each sample, it is assumed that the temperature for each sample is similar. In the work of Berry et al. [35], the temperature dependency of samples with the same matrix composition, but different iron redox states were indeed found to be similar which supports this assumption. Velocity calibration was carried out using an α-Fe foil at room temperature. The experimental Mössbauer spectra were fitted with several doublets using the Mosswinn 4.0 program [39] to best match the experimental spectrum. As each doublet has a characteristic isomer shift δ and quadrupole split Δ, a doublet can be assigned to an iron atom in a certain oxidation state and coordination number, i.e., $^{[Y]}Fe^{x+}$ in which Y is the coordination number and x the oxidation state [33]. Thus, from the area of a doublet, the concentration of an iron atom with a certain oxidation state and coordination number can be calculated.

Wet Chemistry

Wet chemistry methods were carried out by Australian Laboratory Services (ALS) who determined the iron redox state via a combination of direct titration to determine the slag's Fe^{2+} content and XRF analysis to determine the total Fe content. Disks for XRF analysis were prepared via adding some slag (0.66 g) in a platinum crucible together with $Li_2B_4O_7$ and $LiNO_3$ and putting them in a furnace at 1050 °C to be fused. The direct titration method is based on the work of Pratt [40]. 1 g of material is dissolved in an HF–H_2SO_4 mixture in order to release Fe^{2+} from the slag/glass matrix. After the step dissolution, the mixture is complexed with H_3BO_3 and H_3PO_4 and subsequently titrated with $K_2Cr_2O_7$ to determine the amount of Fe^{2+} within the slag. The corresponding reactions are provided hereunder. Based on reference samples, it was determined that the uncertainty of the Fe^{2+}/Fe^{3+} determination from wet chemistry lies around 1–3%.

$$Fe^{2+}_{sample} \overset{H_2SO_4-HF}{\rightarrow} Fe^{2+}_{sol} \quad (2)$$

$$6Fe^{2+} + Cr_2O_7^{2-} + 14H^+ \rightarrow 6Fe^{3+} + 2Cr^{3+} + 7H_2O \quad (3)$$

Preparation of End-Member Standards

Two additional samples with the same target composition as shown in Table 1 were prepared in a separate experimental sequence using a smaller vertical tube furnace. The intent of these experiments was to gain insight into the two iron oxidation state extrema, and thus on the one hand, an atmosphere corresponding to pure oxygen $p_{O2} = 1$ atm was chosen, while on the other hand an atmosphere corresponding to Fe saturation was chosen $p_{O2} = 10^{-11}$ atm. For the given slag, this corresponded to an Fe^{3+}/Fe_{tot} ratio of 0.92 and 0.05, respectively. The idea of analyzing the redox ratio of these samples is to verify whether Mössbauer spectroscopy and/or wet chemistry could have a potential deviation to highly oxidized/highly reduced samples. Samples were prepared using the same approach as for the electrical conductivity experiments, i.e., the CAS sinter was combined with Fe_2O_3 powder (99.8%) and Fe powder (99.9%) to obtain the abovementioned Fe^{3+}/Fe_{tot} ratios. To have sufficient material for both Mössbauer and titration, a total mass of 5 g was prepared per experiment. The mixture was first pelletized using a tool steel die and the resulting pellets were then inserted in an alumina crucible (OD = 10 mm, ID = 8 mm, height = 15 mm). The alumina crucible was suspended in a vertical (resistance) tube furnace via a Kanthal wire. The furnace was first flushed (500 ml/min) for 30 min at 1310 °C with a pure O_2 ($p_{O2} = 1$ atm) or a CO_2–CO–Ar mixture ($p_{O2} = 10^{-11}$ atm) after which the sample was brought up to the hot zone of the furnace and held there for 24 h. At the end, the samples were quenched in a $CaCl_2$ brine solution (− 20 °C). The samples then underwent EPMA, Mössbauer and wet chemistry analyses as described earlier.

Results and Discussion

LOM and Composition Analysis (EPMA and XRF)

Similar as to the previous work [24], the presence and location of solid crystals was determined from LOM analysis. It was found that only the samples with a p_{O2} between 10^{-4} atm and 10^{-6} atm contained solid crystals, which were located at the bottom the crucible. As already described in our previous work [24], these crystals were inferred to be Fe_3O_4–10 mol% $AlO_{1.5}$ particles which are likely formed due to the desired Fe^{3+}/Fe_{tot} content being close to the ideal ratio for these spinels to form. The height of this layer as a function of p_{O2} is given in Table 3. If such a layer of spinel crystals was found in a sample, the sample was cut with a diamond disk saw above this layer and the abovementioned analysis techniques were performed on the homogeneous slag.

The results of the EPMA and XRF slag composition analysis as a function of the applied atmosphere in the furnace are found in Table 4. Regarding the slag's SiO_2, CaO, and 'FeO' content, a difference of about ±1 mol% is observed between both analysis techniques which lies within the range of uncertainties of both methods [41, 42]. On the other hand, for $AlO_{1.5}$, the difference seems to be more significant as it lies around 2–3 mol%. Comparison of the effective measured values versus the target values also reveals that for most atmospheres, the target value is well achieved for SiO_2, CaO, and 'FeO' (±1 mol%) and reasonably achieved for $AlO_{1.5}$ (±2 mol%). The only exception is the slag prepared in a pure oxygen atmosphere [$\log(p_{O2}) = 0$] for which an excessive amount of $AlO_{1.5}$ is observed. This is likely related to the absence of a spinel passivation layer at the slag/crucible interface. However, samples in air and $p_{O2} = 10^{-2}$ atm also did not show any passivation layer, but their $AlO_{1.5}$ content is not substantially higher compared to experiments where a layer was observed. Thus, a second explanation potentially lies in the difference in scale between the experiment prepared in pure oxygen and the conductivity experiments. As already mentioned, the former experiment was carried out with a mass of 5 g, whereas the latter were carried out with approximately 40 g. As a result, it is likely that the sample with a lower mass is more quickly enriched with $AlO_{1.5}$ across the entire sample. For all samples, it is found that the 'FeO' content is below the target ratio, which could stem from iron losses to the crucible through the formation of a passivation layer and iron losses to the loose spinel layer. It is (roughly) estimated (see the online supplementary material) that these iron losses can lead to a decrease in the slag's 'FeO' content by 0.6–1.8 mol% which is similar to the measured deviation from EPMA and XRF.

Fe^{3+}/Fe^{2+} Determination

The iron redox state was determined via both Mössbauer spectroscopy and wet chemistry using titration. First, the results of Mössbauer spectroscopy are discussed. These results are dependent on assumptions regarding the spectrum fitting procedure and potential corrections of the recoilless fraction of Fe^{3+}/Fe^{2+}. Two fitting approaches were used of

Table 3 The height of the solid layer at the bottom of the crucible for the different oxygen partial pressures

$\log(p_{O2})$	− 4.00	− 5.01	− 5.51	− 5.96
h_{layer} (mm)	3.4	1.6	1.6	0.8

Table 4 Chemical composition (mol%) measured by EPMA and XRF for the electrical conductivity samples as a function of the applied p_{O2}

Log(p_{O2}) Log(atm)	Method	SiO_2 (mol%)	CaO (mol%)	'FeO' (mol%)	$AlO_{1.5}$ (mol%)
Target	–	29.75	33.55	20.70	16.00
0	EPMA	27.4 ± 0.2	31.1 ± 0.2	18.9 ± 0.2	22.5 ± 0.7
	XRF	28.6	31.4	19.1	20.9
− 0.68	EPMA	29.8 ± 0.2	33.3 ± 0.1	19.5 ± 0.1	17.5 ± 0.2
	XRF	30.5	33.7	20.2	15.7
− 2	EPMA	29.8 ± 0.5	33.2 ± 0.3	19.3 ± 0.3	17.7 ± 1.0
	XRF	30.9	33.8	20.4	14.9
− 4	EPMA	30.1 ± 0.3	33.7 ± 0.3	19.5 ± 0.3	16.6 ± 0.5
	XRF	31.2	34.5	19.8	14.6
− 5.01	EPMA	29.9 ± 0.3	33.2 ± 0.3	19.7 ± 0.3	17.0 ± 0.5
	XRF	31.0	34.2	20.1	14.6
− 5.51	EPMA	30.2 ± 0.2	33.8 ± 0.2	19.5 ± 0.2	16.4 ± 0.2
	XRF	31.2	34.5	19.8	14.5
− 5.96	EPMA	29.9 ± 0.5	33.5 ± 0.5	19.8 ± 0.7	16.8 ± 0.3
	XRF	31.1	34.1	19.6	15.1
− 6.87	EPMA	30.0 ± 0.2	33.3 ± 0.2	19.5 ± 0.2	17.2 ± 0.1
	XRF	31.1	33.8	20.3	14.8
− 7.92	EPMA	30.0 ± 0.2	33.5 ± 0.2	19.8 ± 0.1	16.7 ± 0.2
	XRF	30.9	33.8	20.6	14.6
− 11	EPMA	29.5 ± 0.4	33.3 ± 0.2	20.1 ± 0.9	17.0 ± 0.5
	XRF	30.4	33.3	20.7	15.5

The target composition is also provided as a reference. For XRF, no standard deviations could be reported as there was only sufficient material for one analysis

which the results can be found in Tables S-I and S-II. The first approach, fit 1, was done via a free, independent fitting procedure in which the isomer shift δ and quadrupole splitting Δ are not fixed. For this procedure, 4 doublets were needed per sample to obtain the best fit with the experimental absorption spectrum. As for the second approach, fit 2, the isomer shift and quadrupole splitting were fixed based on a doublet corresponding to $^{[6]}Fe^{2+}$ in proximity to $^{[6]}Fe^{3+}$, which appears in the Mössbauer spectrum as a doublet corresponding to an Fe cation with an oxidation state of 2.5, i.e., $^{[6]}Fe^{2.5+}$. Such a doublet has been utilized for Mössbauer spectra of magnetite [43] and in the analysis of Mid Ocean Ridge Basalt (MORB) glasses [35]. Physically, the presence of neighboring Fe^{2+} and Fe^{3+} cations in slags can be expected due to the observed clustering behavior of Fe cations as indicated from electron paramagnetic resonance spectroscopy [44–46], optical absorption spectroscopy [47], and neutron diffraction spectroscopy [48–50]. It should be noticed though that the term 'clustering' is simply defined as the presence of two or more 'neighboring' Fe cations, i.e., Fe^{x+}–O–Fe^{y+} bonds (x, $y = 2$ or 3), thus it does not necessarily reflect to regions within the slag that are composed out of solely iron cations. In the current work, the isomer shift and quadrupole split of this doublet was determined based on the sample obtained at a $p_{O2} = 10^{-5.51}$ atm. The isomer shift $\delta = 0.62$ corresponded well with those found by Gorski and Scherer [43] and Berry et al. [35]. In addition, two extra doublets for other Fe^{3+} and Fe^{2+} were necessary as well to obtain a good fit with the experimental spectrum. For each other doublet, the identification of the Fe species in terms of oxidation state and coordination number(s) is made via the work of Murad and Cashion [33]. The quality of the fit was compared for both spectra based on the χ^2 parameter. This indicates that fit 1 corresponds better to the experimental data, which may be related to the free fitting procedure in which agreement with the experimental spectra was prioritized. In that aspect, it is found that the χ^2 values of fit 2 still closely match those of fit 1 (apart from the measurement in air) and thus, the assumption of the clustered doublet is reasonable. From the spectral area of the individual doublets and their assignment to a certain oxidation state of Fe, the Fe^{3+}/Fe^{2+} ratio can be determined. However, the doublet corresponding to $^{[6]}Fe^{2.5+}$ can be interpreted in multiple ways. According to the study of Berry et al. [35], this doublet can be fully assigned to Fe^{2+}, whereas in the study of Gorski and Scherer [43], the contribution of this doublet is divided evenly between Fe^{2+} and Fe^{3+} as the electron hopping between octahedral Fe cations happens faster than the Mössbauer characteristic time. As electrons can jump from one oxidation state to another in glasses, the assignment of

this doublet to both Fe^{2+} and Fe^{3+} is also considered. Therefore, in this work, the former approach is further referred to as fit 2.a and the latter as fit 2.b. Besides the fitting procedure, another important aspect is to check for the temperature dependence of the redox ratio. The Fe^{3+}/Fe^{2+} ratios of the $p_{O2} = 10^{-5.5}$ atm sample as well as the temperature dependency parameter r, defined in Eq. (4), between the Fe^{3+}/Fe^{2+} ratio at temperature T and at room temperature are provided in Table 5**.**

$$r(T) = \frac{Fe^{3+}/Fe^{2+}\,(298\,K)}{Fe^{3+}/Fe^{2+}\,(T)} \tag{4}$$

It is observed that the apparent Fe^{3+}/Fe^{2+} ratios at room temperature are significantly higher than at cryogenic temperatures (50 K, 20 K) for fit 1 and fit 2.b, which is related to the difference in Debye temperature between Fe^{3+} and Fe^{2+} as explained before. However, as the temperature is progressively decreased to cryogenic temperatures, it is found that the ratio becomes nearly constant as little (to no) difference is found between the Fe^{3+}/Fe^{2+} ratios at 50 K and 20 K. For fit 1 and fit 2.b, r values of 1.25 and 1.15 are found, respectively, and as such, a correction procedure for this temperature dependency is made for samples made at other p_{O2}'s, which can be found in Eq. (5). The assumption behind this correction procedure is that for each sample, a similar ratio r should be found as a function of temperature as the matrix composition, i.e., SiO_2, CaO, and $AlO_{1.5}$, between the different samples is nearly identical as shown earlier (the only exception being the sample at $p_{O2} = 1$ atm).

$$Fe^{3+}/Fe^{2+}\,(p_{02},\,20\,K) = \frac{1}{r(20)}\,Fe^{3+}/Fe^{2+}\,(p_{02},\,298\,K) \tag{5}$$

On the other hand, fit 2.a does not show a strong deviation as a function of temperature with r ratios of 1.04 and 1.07. This seems to agree with the observation of Berry et al. [35] who found an r ratio of 1.03 ± 0.03, which is sufficiently low to assume temperature independence. Therefore, no correction procedure was done for fit 2.a. The Fe^{3+}/Fe_{tot} ratios determined from each Mössbauer fitting procedure and those obtained via titration are plotted as a function of the redox ratios predicted by FactSage 7.3 in Fig. 1a. In addition, a second comparison between both measurement methods is done in Fig. 1b. In general, it is observed that the samples are more oxidized, i.e., have a larger Fe^{3+}/Fe_{tot} ratio, compared to the predicted Fe^{3+}/Fe_{tot} ratio, whereas good agreement is found between the titration and Mössbauer method.

In terms of the different fitting approaches, it is observed that fit 1 predicts the highest Fe^{3+}/Fe_{tot} values, whereas fit 2.a predicts the lowest. In addition, it is observed that fit 2.a more closely matches the titration values at more oxidizing conditions, whereas fit 1 and 2.b more closely match those at more reducing conditions (with the exception of 2.b at Fe saturation). However, as the uncertainty on spectral contributions of Mössbauer is typically attributed to be ±5% [47] and χ^2-values between methods are rather similar, it is considered that each fitting procedure falls within this uncertainty range making it difficult to rank them. As a result, from now on, the iron redox state will be reported as an average value from those obtained via Mössbauer and wet chemistry. It was also observed that the Fe^{3+}/Fe^{2+} ratio did

Table 5 Fe^{3+}/Fe^{2+} and temperature dependency parameter obtained for the sample at $p_{O2} = 10^{-5.5}$ atm as a function of the temperature and fitting procedure

	Fit 1		Fit 2.a		Fit 2.b	
T (K)	Fe^{3+}/Fe^{2+}	r	Fe^{3+}/Fe^{2+}	r	Fe^{3+}/Fe^{2+}	r
298	1.57	–	0.88	–	1.27	–
50	1.25	1.25	0.83	1.07	1.11	1.15
20	1.26	1.25	0.85	1.04	1.11	1.15

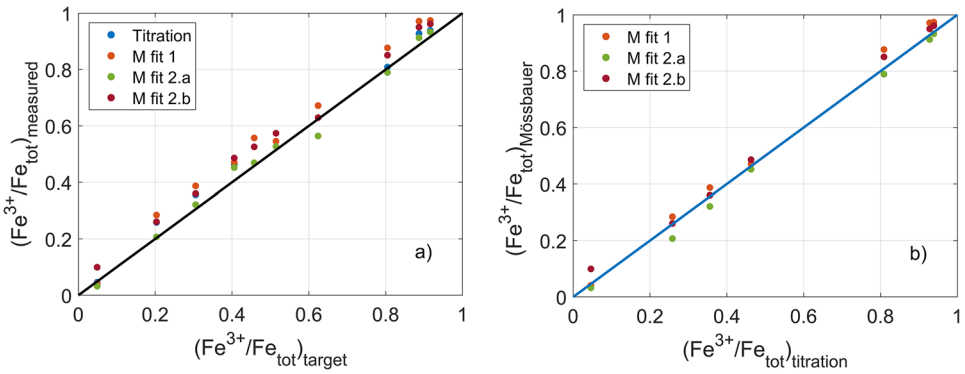

Fig. 1 **a** Comparison of the target Fe^{3+}/Fe_{tot} ratio (mol/mol) with measurements of titration and the various Mössbauer fits (M fit). **b** Comparison of the Fe^{3+}/Fe_{tot} ratio obtained via titration and Mössbauer

not vary significantly across the bath height based on the Mössbauer results of the sample taken at a $\log(p_{O2}) = -2$. From Table S-III, a difference of 1.3% on the Fe^{3+}/Fe_{tot} ratio is observed between the top and bottom of the sample which is within the technique's uncertainty. For the majority of the samples, it is found that the measured Fe^{3+}/Fe_{tot} ratio is higher than the target ratio. A potential explanation is that some iron cations from the slag, both Fe^{2+}/Fe^{3+}, end up either in the spinel passivation layer or in the solid crystals at the bottom. This seems to be consistent with the measured 'FeO' content which is slightly below the target value for most samples as mentioned earlier. A rough estimation on the impact of iron losses on the iron redox ratio (details see the online supplementary material) showed that a deficit in Fe^{2+} is likely the result of an incomplete reaction of metallic Fe and Fe_2O_3. The amount of Fe^{2+} obtained through reaction in Eq. (1) was targeted to match the Fe^{2+} content in the slag and thus did not take into account any losses to the spinel layer/solid crystals, which could explain the observed higher Fe^{3+} content.

More importantly though, a continuous decrease in the Fe^{3+}/Fe_{tot} ratio is found for progressively reducing atmospheres. As the main target of this work is to further understand the relationship between the electrical conductivity and the iron redox state, this controlled decrease in iron redox state is already a first validation that the used methodology is a correct approach in terms of slag preparation and experimental conditions to further test hypotheses on electrical conductivity.

Electrical Conductivity Results

Total Conductivity and Electronic Transference Number

First, the total electrical conductivity is compared with trends from literature and with any uncertainties on the experimental data due to the followed procedure. Figure 2a and b shows the total electrical conductivity as a function of the immersion depth and iron redox state, respectively. From Fig. 2a, it is seen that the total conductivity is independent of the immersion depth. Moreover, this independence is found both for samples where a loose spinel layer at the bottom was observed via LOM and for those where this layer was absent. As already mentioned in our previous work [24], it is expected that this layer has a limited effect on the electrical conductivity due to a limited amount of current reaching this layer.

As expected from the earlier works [15–20], the total conductivity first increases with decreasing Fe^{3+} content until a maximum is reached after which the conductivity slowly decreases but remains higher than at more oxidizing conditions. Although the conductivity maximum is somewhat subtle, from a qualitative perspective, the obtained results agree already with the expected trend when going from an oxidizing to reducing environment. The experimental reproducibility of the high-temperature experiments was found to vary between 3 and 21% as determined from two different experiments. Similar to the previous study [24], additional sources of uncertainty on the experimental data were identified: uncertainty on the thermocouple's reading, changes in slag chemistry due to crucible dissolution, and changes in the Fe^{2+}/Fe^{3+} ratio due to the sample not being in equilibrium with the applied gas atmosphere during the measurement and deviations in the cell geometry between calibration and high-temperature experiments. The former two uncertainties are described to the applied methodology, whereas the latter is inherent to the need for a calibration procedure. As a summary, the uncertainty of each contribution for each condition can be found in Table S-VI. The impact of changes in the slag composition on the electrical conductivity was found to be limited as the difference in electrical conductivity before and after an SPC measurement step (40 min)

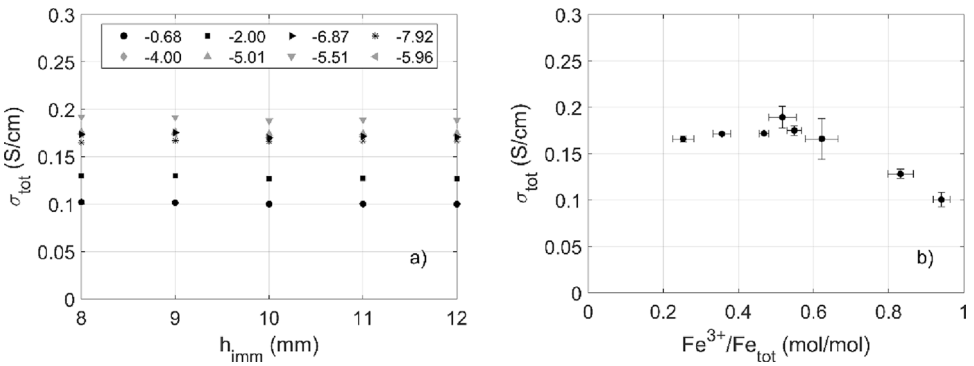

Fig. 2 **a** Total conductivity (S/cm) for the different applied oxygen partial pressures [$\log(p_{O2})$] as a function of the immersion depth. Grey datapoints indicate conditions for which a loose spinel layer was found at the bottom, whereas black datapoints indicate the absence of such a spinel layer. **b** Total conductivity as a function of the average Fe^{3+}/Fe_{tot} redox state obtained via titration and Mössbauer spectroscopy. The error bars on the iron redox state and electrical conductivity indicate 1 standard deviation (Color figure online)

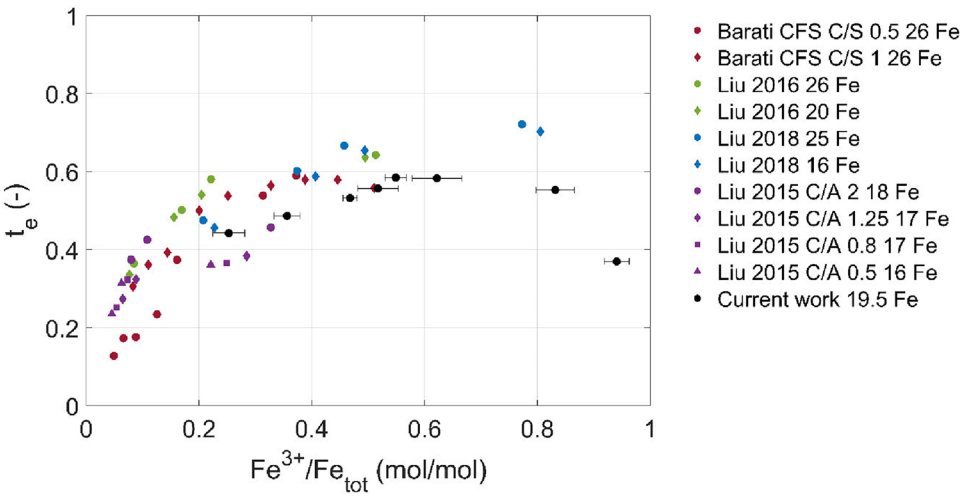

Fig. 3 Electronic transference number as a function of the iron redox state Fe^{3+}/Fe_{tot} obtained via Mössbauer and titration (present work) or predicted via FactSage 7.3 (UQPY) [25, 51] using the experimental conditions (temperature, p_{O2}) reported in literature [17–20]. Error bars for the present work indicate one standard deviation. C/S indicates the CaO/SiO_2 ratio in wt%, whereas C/A indicates the CaO/Al_2O_3 ratio in mol%

was about 1.2%–4.7%. In addition, as mentioned in section "LOM and composition analysis (EPMA and XRF)", the total increase of the slag's $AlO_{1.5}$ content over the entire experiment is only around ±2 mol% (from EPMA results), while from the section "Fe3+/Fe2+ determination" it is likely that the difference in Fe^{3+}/Fe_{tot} content across the bath height is negligible. This indicates that the slag composition is sufficiently stable within the timeframe of the measurements and thus that the measured conductivity values are representative for the slag composition as analyzed.

The electronic transference number as a function of the iron redox state is provided in Fig. 3 for the obtained data in this work and for several other literature studies [17–20]. For the present data, the transference number was reproducible within a 3% range. The iron redox ratio Fe^{3+}/Fe_{tot} for the literature studies were estimated via FactSage 7.3 UQPY database [25] using the provided slag compositions, temperature, and p_{O2}. It was found by these studies [17–20] that electronic transference numbers are independent of temperature[2] and thus they provide an easy way of comparing experimental data. For the investigated conditions in the present work, t_e varies between 0.37 and 0.58 which implies that between 37 and 58% of the current is transported via the electron hopping mechanism. As shown in Fig. 3, these orders of magnitude are comparable with literature data which have similar 'FeO' concentrations. From this observation, it can already be concluded that the addition of 'FeO' to a silicate melt can drastically increase the electrical conductivity.

Ionic Conductivity

The ionic conductivity as a function of the iron redox state Fe^{3+}/Fe_{tot} is shown in Fig. 4 along with the predicted ionic conductivity from the model from Thibodeau [52]. Similar to results from literature [17–20], a linear dependency of the ionic conductivity as a function of the iron redox state is found. As expected, the ionic conductivity increases with decreasing Fe^{3+}/Fe_{tot} ratio as the mobility of Fe^{2+} is considered significantly higher than that of Fe^{3+}. As a first estimation of which cations contribute to the ionic conductivity, the effective diffusion coefficients of all cations are calculated using the model of Thibodeau [52]. The diffusion coefficients of Ca^{2+} and Fe^{2+} for the present system are of an order 10^{-6} and 10^{-5} cm^2/s, respectively, whereas

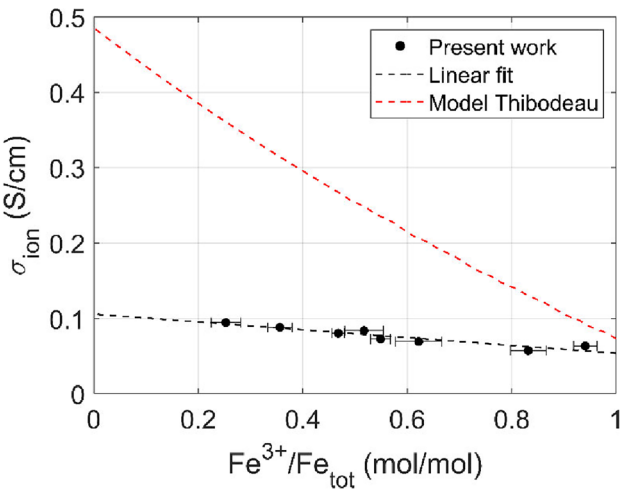

Fig. 4 Ionic conductivity as a function of the iron redox state Fe^{3+}/Fe_{tot}. Error bars indicate one standard deviation. As a comparison, the ionic conductivity as predicted by the model of Thibodeau [52] is included as well

[2] Provided that the iron concentration is still sufficiently low such that electronic conduction is still limited by Fe^{2+} diffusion.

for Al^{3+} and Fe^{3+}, the diffusion coefficient was of an order 10^{-8} cm^2/s. Thus, the Nernst–Einstein expression for iron silicate melts can be further simplified to Eq. (6). Within this equation, σ_{ion} (S/cm) is the ionic conductivity, F (C/mol) is Faraday's constant, R (J mol^{-1} K^{-1}) is the universal gas constant, T (K) is the temperature, D_i (cm^2/s) is the diffusion coefficient of cation i, $[i]$ (mol/cm^3) is the concentration of cation i, and y (-) is the Fe^{3+}/Fe_{tot} ratio.

$$\sigma_{ion} = \frac{4F^2}{RT}\left(D_{Ca2+}\left[Ca^{2+}\right] + D_{Fe2+}[Fe] \times (1-y)\right). \quad (6)$$

Ionic conduction in slags occurs through an ion hopping mechanism, which can be seen as one cation entering the vacancy that was previously occupied by another cation that is pushed out of its original position due to this motion [53, 54]. Thus, ionic conduction is hindered either by an increased degree of polymerization as less suitable hopping spots are available, through immobilization of network breaking cations as a result of charge compensation [55] or via a mismatch in hopping spots from different cations, i.e., the mixed-modifier effect [56, 57]. Therefore, in order for Eq. (6) to be linear as a function of the ferric ratio, the diffusion of Ca^{2+} and Fe^{2+} should be independent of the Fe^{3+} content, i.e., the presence of Fe^{3+} should not hinder the movement of other cations due to either an increase in the degree of polymerization or via the immobilization of network breaking cations through charge compensation. In addition, any decrease in ionic conductivity due to mixed-modifier effects because of differences in the local environments of Ca^{2+} and Fe^{2+} should be sufficiently small (or non-existent).

First, it will be deduced that Fe^{3+} is unlikely to hinder the movement of more mobile cations such as Ca^{2+} and Fe^{2+}. In slags, it is found that Fe^{3+} can act either as a (weak) network former ($^{[4]}Fe^{3+}$) or network modifier ($^{[6]}Fe^{3+}$) depending on whether it can be incorporated in the silicate network via charge compensation [58]. In case of charge compensation, Fe^{3+} keeps a Ca^{2+} cation close in its environment to obtain a 4+ oxidation state which allows a tetrahedral configuration similar to the silicon cations Si^{4+}. As a result, Ca^{2+} might be more strongly bound in this charge compensation site, than as if it were bound to oxygen anions as a network modifier, thus its mobility could be decreased [55]. However, as shown in Tables S-I and S-II, it is not possible to discern between the Fe^{3+} coordination states from the fitted doublets of Mössbauer spectroscopy, which may be expected given that a slag is inherently unorganized. An estimation of the likelihood that an Fe^{3+} cation could be charge-compensated by Ca^{2+} may be found from the viscosity model of Kim et al. [59]. In their work, the Gibbs free energy $\Delta G_{CaFe2O4}$ (J/mol) of the charge compensation reaction, Eq. (7), is estimated via predicting the experimentally observed viscosity maximum as a function of the slag's Fe_2O_3 content. In their work, they assumed this Gibbs free energy to be a function of the slag's silica content, X_{SiO2}, as shown in Eq. (8).

$$2Fe^{3+}O_{1.5} + CaO \rightleftarrows CaFe_2O_4 \quad (7)$$

$$\Delta G_{CaFe2O4} = 2092 - 5335X_{SiO2} \quad (8)$$

For the present work, $\Delta G_{CaFe2O4} > 0$ and thus, it is considered unlikely that Fe^{3+} is charge compensated by Ca^{2+}, under which circumstances it would restrict the movement of Ca^{2+} cations and increase the slag's degree of polymerization. Therefore, as Fe^{3+} is progressively replaced by Fe^{2+} within the slag at more reducing conditions, only the amount of mobile cations and ion hopping sites increases, while the ion hopping mechanism, i.e., diffusion of Ca^{2+} and Fe^{2+} throughout the matrix, remains unaffected.

As for the influence of a mixed-modifier effect between Fe^{2+} and Ca^{2+}, an indication for this effect may have been observed by Wejnarth [60] as a non-linear decrease of the electrical conductivity was observed when replacing Fe^{2+} with Ca^{2+} for a constant amount of SiO_2. However, this decrease could also stem from a loss in electronic conduction, as no distinction was made between the two contributions. In the current dataset, although a slight decrease in the ionic conductivity is observed between the measurement in air ($Fe^{3+}/Fe_{tot} = 0.94$) and the one in an atmosphere of $p_{O2} = 10^{-2}$ atm ($Fe^{3+}/Fe_{tot} = 0.83$), the overall observed trend is considered to be linear. Therefore, it is believed that any decrease in ionic conduction due to a mismatch between Ca^{2+}/Fe^{2+} sites is negligible compared to the increase of mobile cations and hopping sites.

As for the ionic contribution of Fe^{2+}, our experimental data deviate strongly from the conductivity model of Thibodeau as the latter predicts a much stronger increase with increasing Fe^{2+} content. This difference can be explained via comparison of the Ca^{2+} and Fe^{2+} diffusion coefficients of the experimental data and of the model. The experimentally derived diffusion coefficients are estimated via assuming a linear fit of the measured data according to Eq. (6). The dependency as a function of the Fe^{3+}/Fe_{tot} ratio y is shown in Eq. (9) ($R^2 = 0.88$).

$$\sigma_{exp}(y) = 0.106 - 0.052y \quad (9)$$

Combination of the above linear fit and Eq. (6) allows to calculate the diffusion coefficients of Ca^{2+} and Fe^{2+}, respectively, as follows:

$$D_{Ca^{2+}} = \frac{\sigma_{exp}(y=1)}{\left[Ca^{2+}\right]} \times \frac{RT}{4F^2} \quad (10)$$

Table 6 $Ca^{2+}$and Fe^{2+} diffusion coefficients derived from the obtained experimental data and calculated from the model of Thibodeau [52]

	Experimentally derived	Thibodeau
$D_{Ca^{2+}}$(cm²/s)	$1.43 \cdot 10^{-6}$	$1.79 \cdot 10^{-6}$
$D_{Fe^{2+}}$(cm²/s)	$1.53 \cdot 10^{-6}$	$1.32 \cdot 10^{-5}$

$$D_{Fe^{2+}} = \left(\sigma_{exp}(y=0) - \frac{4F^2}{RT}\left[Ca^{2+}\right]D_{Ca^{2+}}\right) \times \frac{RT}{4F^2} \times \frac{1}{\left[Fe^{2+}\right]} \quad (11)$$

Both diffusion coefficients are shown in Table 6. It is observed that both the experimentally derived and the model's Ca^{2+} diffusion coefficient D_{Ca2+} are nearly equal which is consistent with the electrical conductivity data given that both the experimental data and the model data seem to (nearly) converge at $Fe^{3+}/Fe_{tot} = 1$. On the other hand, the experimentally derived D_{Fe2+} differs by a factor 10 with the one obtained by the model. Moreover, it is found from the experimental data that the diffusion coefficients of Fe^{2+} are only slightly larger than that of Ca^{2+}. It is expected from literature [55, 11] that a cation's contribution to the ionic conductivity increases as its ionic radius decreases, which is consistent with the obtained diffusion coefficients for Ca^{2+} (114 pm) and Fe^{2+} (92 pm) [61]. Moreover, Barati and Coley [22] did a similar analysis of their ionic conductivity data for a SiO_2–CaO–'FeO' system and found that the Fe^{2+} diffusion coefficient is about twice that of Ca^{2+}. Therefore, it is assumed that the diffusion coefficient predicted by the model of Thibodeau is an overestimation. This overestimation may stem from the author using binary SiO_2–'FeO' electrical conductivity data, thus without separation of ionic and electronic contributions, with relatively high 'FeO' content (> 55 mol%) at iron saturation for the estimation of the model parameters for D_{Fe2+}. From the study of Simnad et al. [62], it is found that even at iron saturation, a significant portion of the current will be conducted via electrons if the 'FeO' content in a SiO_2–'FeO' is above 70 mol%, which may lead to an overestimation of the ionic conduction attributed to Fe^{2+}. This reasoning is consistent with the observation that their model overestimates the electrical conductivity of iron containing melts of higher order systems.

Electronic Conductivity

As a final part of the analysis of the conduction mechanism, the electronic conductivity is analyzed as a function of the measured iron redox ratio Fe^{3+}/Fe_{tot} as shown in Fig. 5. In addition, the gathered experimental data are compared to several models. When looking at the experimental data, the electronic conductivity inclines toward a parabolic dependency as a function of Fe^{3+}/Fe_{tot} with a maximum near an Fe^{3+}/Fe_{tot} ratio of 0.5 as this signifies the ideal ratio of an equal number of electron donating (Fe^{2+}) and electron accepting (Fe^{3+}) cations. This is consistent with the current theories from literature [15, 22] and thus, as a first model, a simple parabolic fit, Eq. (12), is proposed. For the present data, the fitting parameter A was found to be equal to 0.41 S/cm and an $R^2 = 0.89$ was found.

$$\sigma_{el,simple}(y) = A \bullet y(1-y) \quad (12)$$

Besides the simple parabolic model, an attempt was also made to fit our data with the structural DACT model developed by Barati and Coley [22] for which the full expression is given in Eq. (13).

$$\sigma_{el,DACT}(y) = 4\pi N_a \frac{r^0 (r^*)^3}{r^0 - r^*} \frac{F^2}{RT} D_{Fe^{2+}} [Fe]^2 y(1-y) \quad (13)$$

This model assumes that electronic conduction occurs via a two-step process in which Fe^{2+} cations first diffuse toward Fe^{3+} centers until they are at an optimum e^- hopping distance r^*. In the work of Barati and Coley, this parameter r^* was fitted with their experimental data and they found a value of 3.87 Å. A second assumption of the model is that the Fe cations are distributed homogeneously within the melt and are located at a distance r^0 from each other, which is calculated via the slag's molar volume V_m, the 'FeO' mole fraction X_{Fe}, and Avogadro's number N_a, Eq. (14).

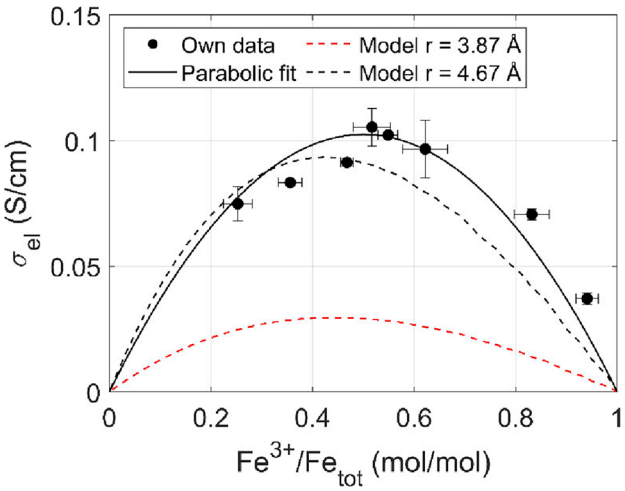

Fig. 5 Electronic conductivity as a function of the measured iron redox ratio Fe^{3+}/Fe_{tot} (error bars indicate one standard deviation). The experimental data are modeled via a simple Parabolic fit (quadratic dependency) and via the model proposed by Barati and Coley [22] for their experimentally determined optimal e^- hopping distance r^* (3.87 Å) and for the r^* value for which the best agreement was found for our data (4.67 Å)

$$r^0 = \left(\frac{V_m}{N_a.X_{Fe}}\right)^{1/3} \quad (14)$$

In the current work, the slag molar volume was estimated via the molar volume model of Thibodeau et al. [26–28] as a function of the iron redox ratio. As seen from Fig. 5, the obtained experimental data are poorly predicted via the DACT model with $r^* = 3.87$ Å. Therefore, the parameter r^* was optimized to best value representing the current experimental data and a value of 4.67 Å was found with $R^2 = 0.70$. This would suggest though that the optimal e^- hopping distance r^* varies (strongly) as a function of the slag composition. A potential reason for this variation in the r^* parameter may be related to the influence of the matrix components (SiO_2, CaO, $AlO_{1.5}$) on the Fe^{2+}/Fe^{3+} environment/electron charge density which could affect optimum e^- hopping distance r^*. This hypothesis should be checked for more experimental data though, but it was considered to be beyond the scope of the current work.

Conclusion

Electric furnaces will play an important role in future metal production techniques. In order to design and operate these furnaces properly, electrical conductivity data are extremely important. The present work investigated the electrical conductivity in combination with the SPC of an SiO_2–CaO–$AlO_{1.5}$–'FeO' system at a constant temperature as a function of the Fe^{3+}/Fe_{tot} ratio. Contrary to previous work, the iron redox state was experimentally determined via combining Mössbauer spectroscopy and wet chemistry. A continuous decrease in Fe^{3+}/Fe_{tot} ratio was found which varies accordingly to the different atmospheres applied during each experiment which confirmed that the changes in the electrical conductivity are attributed to a difference in the sample's iron redox state. The total electrical conductivity as a function of the iron oxidation state showed a (subtle) maximum as a function of the iron redox state. In addition, the obtained electronic transference numbers agreed with those obtained from literature studies which investigated slags with a similar iron content. For the ionic conductivity, a linear increase was found with a decreasing Fe^{3+}/Fe_{tot} ratio due to the increased mobility of the Fe^{2+} cation compared to the Fe^{3+} cation. Moreover, it was deduced that Fe^{3+} is unlikely to hinder cation movement via the charge compensation effect. The trends on the derived diffusion coefficients for Ca^{2+} and Fe^{2+} were found to be consistent with the studies in literature. However, the current structural ionic conductivity model is unable to reproduce our results. For the electronic conduction, a parabolic trend as a function of the iron redox state is found with a maximum near $Fe^{3+}/Fe_{tot} = 0.5$. The DACT model was tested for the experimental data obtained in this work. It was found that the model parameter r^* needed to be adapted to 4.67 Å instead of the model's original 3.87 Å to estimate the order of magnitude of the current results. This may imply that the r^* parameter is dependent on the slag's composition as well. Therefore, in order to optimize any electrical conductivity models of iron silicate slags, further experimental studies are required which combine electrical conductivity and SPC measurements with analysis techniques to determine Fe^{3+}/Fe^{2+} ratios.

Supplementary Information The online version contains supplementary material available at https://doi.org/10.1007/s40831-025-01308-8.

Acknowledgements P.J. Boeykens holds a grant [HBC.2020.2248] which is supported by VLAIO, the Flanders Innovation & Entrepreneurship Agency, in co-operation with Umicore N.V. I. Bellemans holds a grant from the Research Foundation Flanders [1239024N]. The authors would like to express their thanks to R. Starykh for aiding in the construction of the electrical conductivity setup and for EPMA measurements and to I. Dugulan for his aid with the Mössbauer spectroscopy experiments. This research was supported by the seed grant funding of the Ghent University Special Research Fund, in the frame of the partnership between the University of Queensland and Ghent University.

Declarations

Conflict of interest On behalf of all authors, the corresponding author states that there is no conflict of interest.

References

1. Kirschen M, Hay T, Echterhof T (2021) Process improvements for direct reduced iron melting in the electric arc furnace with emphasis on slag operation. Processes 9:1–10
2. Dalvi AD (2023) Decarbonization of mining and metals industry. A critical overview. Proceedings of the 61st Conference of Metallurgists, COM 2022 1: 917–937
3. Cavaliere P, Perrone A, Silvello A, Stagnoli P, Duarte P (2022) Integration of open slag bath furnace with direct reduction reactors for new-generation steelmaking. Metals. https://doi.org/10.3390/met12020203
4. Shahabuddin M et al. (2024) The performance and charge behaviour in melter/smelter for the production of hot metal in hydrogen DRI-based steelmaking. Ironmak Steelmak Processes, Prod Appl https://doi.org/10.1177/03019233241265179
5. Lötter GJ, Van Niekerk AA, Farmer GE (2021) Pig iron production (post blast furnace era). in Proceedings of the 16th International Ferro-Alloys Congress (INFACON XVI) 2021
6. Palovaara P, Pisilä S, Sakaranaho M, Lindvall M, Tikka J (2021) Benchmarking of FeNi electric arc furnace operations for developing furnace design parameters for lateritic ores in the intermediate SiO2/MgO range of between 2.2 and 2.7. in *Infacon XVI: International Ferro-Alloys Congress*
7. Voermann N, Gerritsen T, Candy I, Stober F, Matyas A (2004) Developments in furnace technology for ferronickel production. in Proceedings of the 10th Int. Ferroalloys Congress
8. Grzella J et al (2003) Metallurgical furnaces. Ullmann's Encycl Ind Chem. https://doi.org/10.1002/14356007.b04_339

9. Friedrich B et al (2018) The submerged arc furnace (SAF): state-of-the-art metal recovery from nonferrous slags. J Sustain Metall 4:77–94
10. Pauna H et al (2020) Electric arc length-voltage and conductivity characteristics in a pilot-scale AC electric arc furnace. Metall Mater Trans B 51:1646–1655
11. Bockris JOM, Kitchener JA, Ignatowicz S, Tomlinson JW (1952) Electric conductance in liquid silicates. Trans Faraday Soc 48:75–91
12. Inouye H, Tomlinson JW, Chipman J (1953) The electrical conductivity of wüstite melts. Trans Faraday Soc 49:796–801
13. Fedor J (1990) Electrical conductivity of melts in the system Fe_2O_3–FeO–CaO. ECS Proc Vol 1990–17:203–210
14. Danek V, Licko T, Panek Z (1986) Conductivity of melts in the system CaO–FeO–Fe_2O_3–SiO_2. Chem Pap 40:215–223
15. Engell H-J, Vygen P (1968) Ionen- und Elektronenleitung in CaO–FeO–Fe_2O_3–SiO_2-Schmelzen. Ber Bunsenges Phys Chem 72:5–12
16. Hundermark R (2003) The electrical conductivity of melter type slags. Preprint at https://open.uct.ac.za/items/adf535b3-3dc0-47ed-b125-a56a5619147f (2003).
17. Barati M, Coley KS (2006) Electrical and electronic conductivity of CaO–SiO_2–FeO_x slags at various oxygen potentials: Part I. Experimental results. Metall Mater Trans B 37:41–49
18. Liu YX, Liu JH, Zhang GH, Zhang JL, Chou KC (2018) Experimental study on electrical conductivity of FexO–CaO–SiO_2–Al_2O_3 system at various oxygen potentials. High Temp Mater Processes 37:121–125
19. Liu JH, Zhang GH, Chou KC (2015) Electronic/ionic properties of FexO–SiO_2–CaO-Al_2O_3 slags at various oxygen potentials and temperatures. ISIJ Int 55:2325–2331
20. Liu JH, Zhang GH, Wu YD, Chou KC (2016) Study on electrical conductivity of FexO–CaO–SiO_2–Al_2O_3 slags. Can Metall Q 55:221–225
21. Zhao B, Jak E, Hayes P, Font J, Moyano A (2009) Viscosity and electrical conductivity of copper slag at controlled oxygen potential. in *Molten 2009: Proceedings of the VIII International Conference on Molten Slages, Fluxes and Salt* 225–235.
22. Barati M, Coley KS (2006) Electrical and electronic conductivity of CaO–SiO_2–FeOx slags at various oxygen potentials: Part II. Mechanism and a model of electronic conduction. Metall Mater Trans B 37:41–49
23. Britten SC, Pal UB (2000) Solid-state amperometric sensor for the in-situ monitoring of slag composition and transport properties. Metall Mater Trans B 31:733–753
24. Boeykens P-J et al (2024) Methodology development of electrical conductivity measurements for iron silicate slags. J Sustain Metall. https://doi.org/10.1007/s40831-024-00985-1
25. Jak E, Shishin D, Shevchenko M, Hayes P (2022) Integrated Experimental Phase Equilibria and Thermodynamic Modelling Research and Implementation in Support of Pyrometallurgical Copper Processing. in *11th International Conference on Copper* 608–634 (Instituto de Ingenieros de Minas de Chile, Santiago, Chile, 2022).
26. Thibodeau E, Gheribi AE, Jung IH (2016) A structural molar volume model for oxide melts part I: Li_2O–Na_2O–K_2O–MgO–CaO–MnO–PbO–Al_2O_3–SiO_2 melts—binary systems. Metall Mater Trans B 47:1147–1164
27. Thibodeau E, Gheribi AE, Jung IH (2016) A structural molar volume model for oxide melts part III: Fe oxide-containing melts. Metall Mater Trans B 47:1187–1202
28. Thibodeau E, Gheribi AE, Jung IH (2016) A structural molar volume model for oxide melts part II: Li_2O–Na_2O–K_2O–MgO–CaO–MnO–PbO–Al_2O_3–SiO_2 melts—ternary and multicomponent systems. Metall Mater Trans B 47:1165–1186
29. Goldman DONS (1983) Oxidation Equilibrium of Iron in Borosilicate Glass. J Am Ceram Soc 66: 205–209
30. Pommier A, Gaillard F, Pichavant M (2010) Time-dependent changes of the electrical conductivity of basaltic melts with redox state. Geochim Cosmochim Acta 74:1653–1671
31. Vergote O, Cnockaert V, Vrielinck H, Bellemans I, Verbeken K (2021) Experimental investigation of the oxidation kinetics of molten lead silicate slags. in Molten 2021, 11th International Conference on Molten Slags, Fluxes and Salts, Abstracts.
32. Mysen BO (2006) The structural behavior of ferric and ferrous iron in aluminosilicate glass near meta-aluminosilicate joins. Geochim Cosmochim Acta 70:2337–2353
33. Murad E, Cashion J (2004) Mössbauer spectroscopy of environmental materials and their industrial utilization. Mössbauer Spectroscopy of Environmental Materials and Their Industrial Utilization Springer. https://doi.org/10.1007/978-1-4419-9040-2.
34. Jayasuriya KD, O'Neill HSC, Berry AJ, Campbell SJ (2004) A Mössbauer study of the oxidation state of Fe in silicate melts. Am Mineral 89:1597–1609
35. Berry AJ, Stewart GA, O'Neill HSC, Mallmann G, Mosselmans JFW (2018) A re-assessment of the oxidation state of iron in MORB glasses. Earth Planet Sci Lett 483:114–123
36. Ottonello G, Moretti R, Marini L, Zuccolini MV (2001) Oxidation state of iron in silicate glasses and melts: a thermochemical model. Chem Geol. https://doi.org/10.1016/S0009-2541(00)00314-4
37. Righter K et al (2013) Redox systematics of martian magmas with implications for magnetite stability. Am Mineral 98:616–628
38. Zhang HL (2022) Advances of ferrous and ferric Mössbauer recoilless fractions in minerals and glasses. Geosci Front 13
39. Klencsár Z (1997) Mössbauer spectrum analysis by evolution algorithm. Nucl Instrum Methods Phys Res B 129:527–533
40. Pratt JH (1894) On the determination of ferrous iron in silicates. Am J Sci s3–48: 149–151
41. Llovet X, Moy A, Pinard PT, Fournelle JH (2021) Electron probe microanalysis: A review of recent developments and applications in materials science and engineering. Progress Mater Sci https://doi.org/10.1016/j.pmatsci.2020.100673
42. Richard D, Rousseau R (2001) Detection limit and estimate of uncertainty of analytical XRF results. Rigaku J 18
43. Gorski CA, Scherer MM (2009) Influence of magnetite stoichiometry on FeII uptake and nitrobenzene reduction. Environ Sci Technol 43:3675–3680
44. Dantas NO et al (2012) Magnetic and optical investigation of $40SiO_2{\cdot}30Na_2O{\cdot}1Al_2O_3{\cdot}(29 - X)B_2O_3{\cdot}xFe_2O_3$ glass matrix. Solid State Sci 14:1169–1174
45. Cnockaert V et al (2020) Quantification of the Fe^{3+} concentration in lead silicate glasses using X-band CW-EPR. J Non-Cryst Solids 536:120002
46. Cnockaert V et al (2021) Determination of the Fe^{3+}/Σ Fe ratio in synthetic lead silicate slags using X-band cw-epr. J Sustain Metall 7:519–536
47. Bingham PA, Parker JM, Searle T, Williams JM, Fyles K (1999) Redox and clustering of iron in silicate glasses. J Non-Cryst Solids 253:203–209
48. Weigel C, Cormier L, Calas G, Galoisy L, Bowron DT (2008) Nature and distribution of iron sites in a sodium silicate glass investigated by neutron diffraction and EPSR simulation. J Non-Cryst Solids 354:5378–5385
49. Weigel C, Cormier L, Calas G, Galoisy L, Bowron DT (2008) Intermediate range order in (Fe,Al) silicate network glasses: a neutron diffraction and EPSR modeling investigation. https://doi.org/10.48550/arXiv.0805.1853.
50. Weigel C et al (2006) Determination of Fe^{3+} sites in a $NaFeSi_2O_6$ glass by neutron diffraction with isotopic substitution coupled with numerical simulation. Appl Phys Lett. https://doi.org/10.1063/1.2359532

51. Bale CW et al (2016) FactSage thermochemical software and databases, 2010–2016. Calphad 54:35–53
52. Thibodeau ER (2014) Modeling the Molar Volume and Electrical Conductivity of Oxide Melts. 170
53. Bunde A, Ingram BMD, Maass P (1994) The dynamic structure model for ion transport in glasses. J Non Cryst Solids 172: 1222–1236
54. Dyre JC, Maass P, Roling B, Sidebottom DL (2009) Fundamental questions relating to ion conduction in disordered solids. Rep Prog Phys. https://doi.org/10.1088/0034-4885/72/4/046501
55. Mills KC, Hayashi M, Wang L, Watanabe T (2013) The structure and properties of silicate slags. Treatise on Process Metallurgy 1: 149–286
56. Kim K-D (1996) Electrical conductivity in mixed-alkali aluminosilicate melts. J Am Ceram Soc 79:2422–2428
57. Boeykens P-J, Van den Bulck A, Scheunis L, Bellemans I, Verbeken K (2024) Electrical conductivity measurements in ternary SiO_2–PbO–CaO slags. Metall Mater Trans B 55:4997–5007
58. Mysen B, Richet P (2005) Silicate glasses and melts. Elsevier, Amsterdam
59. Kim W, Hudon P, Jung I (2021) Calphad modeling the viscosity of silicate melts containing Fe oxide: FeO/Fe_2O_3 containing system. Calphad 72:102244
60. Wejnarth A (1934) The current-conducting properties of slags in electric furnaces: Part I. Trans Electrochem Soc 65:177
61. Shannon RD (1976) Revised effective ionic radii and systematic studies of interatomic distances in halides and chalcogenides. Acta Crystallogr Sect A 32:751–767
62. Simnad MT, Derge G, George I (1954) Ionic nature of liquid iron-silicate slags. JOM 6:1386–1390